

基于百太瓦级激光系统驱动的高能量 13 nm 波段 高次谐波产生

高记星^{1,2}, 娄智远^{1,2}, 杨帆^{1,2}, 杨晓骏¹, 许毅^{1,2}, 冷雨欣^{1,2}, 郑颖辉^{3*}, 曾志男³, 李儒新^{1,2,3}

¹中国科学院上海光学精密机械研究所强场激光物理国家重点实验室, 上海 201800;

²中国科学院大学材料科学与光电工程中心, 北京 100049;

³张江实验室, 上海 201210

摘要 利用百太瓦级激光系统在氦气(Ne)中得到基于高次谐波产生的极紫外脉冲。通过松聚焦结构在 13 nm 波段产生单级次单脉冲能量为 13.5 nJ (13.1 nm 波长)和 11.1 nJ (13.5 nm 波长)的高次谐波辐射,转换效率为 3.6×10^{-7} 和 3.0×10^{-7} ,谐波发散角的半高全宽为 0.32 mrad 和 0.33 mrad。对含时薛定谔方程进行数值求解,得到单原子偶极发射谱,结合麦克斯韦方程组模拟传播效应,同时考虑气体对谐波的吸收效应,理论模拟得到的信号强度随气压和光强的变化趋势与实验结果基本符合。实现相位匹配的谐波光束质量很好,纵向空间分布为高斯型。结合相位匹配条件和空间分布的分析得到了目前激光参数下的最优相位匹配条件。这种基于高次谐波机制的高能量相干极紫外光源在作为自由电子激光的种子光源以及超快非线性实验和半导体工业检测等方面具有广阔的应用前景。

关键词 极紫外; 高次谐波; 相位匹配; 空间分布

中图分类号 O437 **文献标志码** A

DOI: 10.3788/AOS231482

1 引言

近年来,随着高次谐波相干光源和阿秒脉冲^[1-2]研究的迅速发展,它们在自由电子激光种子注入^[3-4]、时间分辨的角分辨光电子谱测量^[5]及无损纳米结构检测^[6]等方面引起了广泛的关注。产生极紫外光源的方式有很多,除了高次谐波产生(HHG),同步辐射^[7]、自由电子激光^[8-10]和激光等离子体^[11-13]等也可产生极紫外光源。相比其他光源,高次谐波具有相干性好、脉冲持续时间短和装置易于小型化等特点。因此,高次谐波机制已经被广泛用于产生极紫外波段相干光源^[14-19]。

对于光源的应用来说至关重要的是获得高转换效率的 HHG,以实现大能量的极紫外脉冲产生。HHG 的微观机制可以用半经典的三步模型^[20]来解释,在该模型中,当激光场前沿有原子到达时,激光场会压缩原子的库仑势,使电子穿过库仑势垒成为自由电子,并在激光场中加速获得能量。当激光场改变方向时,电子返回原子并通过辐射谐波光子释放额外的能量。半经典理论为 HHG 的物理基础提供了直观的图像。从宏观角度来看,激光场沿其传播路径与大量气体原子相互作用,因此,驱动激光和高次谐波之间的相位匹配对

于实现极紫外光源的有效生成来说至关重要^[21]。到目前为止,国际上多个研究小组已经为提高 HHG 的转换效率和脉冲能量作出了很多努力。例如:Takahashi 等^[22]通过优化泵浦脉冲的波前相位实现了低发散角的相干极紫外辐射,在 13.5 nm 波长处的单发脉冲能量约为 25 nJ,转换效率为 5×10^{-7} 。Rudawski 等^[23]在氩气(Ar)和氦气(Ne)中分别产生了 250 nJ (38 nm 波长)和 5 nJ (20.5 nm 波长)的高能量极紫外光源。2018 年,Wang 等^[24]通过优化入射激光波前相位,在 Ar 中产生了 30 nm 波段能量为 0.3 μ J 的极紫外辐射。随后该研究小组于 2020 年^[25]进一步优化波前相位,在离焦位置实现了更好的光束质量,将 25 TW 的驱动激光由焦距为 25 m 的聚焦镜聚焦至 Ar 中,获得了 30 nm 波段 5.6 μ J 的极紫外高能脉冲能量。上述方案中,针对 13 nm 波段采用的是重复频率为 10 Hz 的太瓦级激光系统,产生的谐波转换效率为 5×10^{-7} 。本工作采用自主研发的重复频率为 1 Hz 的 200 TW 钛宝石激光系统^[26],与峰值功率为几个太瓦的激光系统相比,百太瓦激光系统光束的空间质量容易发生退化^[25,27],实验过程要求保持高质量、高功率激光束的持续输出。最高单脉冲能量可达 8 J、驱动激光分束后 7.9 J 的主脉冲能量输送至自由电子激光实验,用于基于激光尾波场

收稿日期: 2023-08-29; 修回日期: 2023-10-11; 录用日期: 2023-10-21; 网络首发日期: 2023-11-01

基金项目: 国家自然科学基金(11127901, 91950203, 11874374)、中国科学院战略性先导科技专项(XDB16)

通信作者: *zhengyh@zjlab.ac.cn

加速机制的电子束源产生^[11]。第二束激光用于高次谐波产生实验,压缩后可实现 1.3 TW 的峰值功率。高次谐波产生实验和自由电子激光实验是同步进行的,目的是与自由电子激光驱动光同源,便于未来将电子束和极紫外种子光源同时注入波荡器中,在自由电子激光放大过程中通过高次谐波种子光源进行调制^[3,25],产生全相干极紫外或 X 射线激光。

利用上述驱动激光获得了高能极紫外脉冲,在 11.6~19.5 nm 波长光谱范围内产生的单脉冲能量为 78.7 nJ。13 nm 波段,即 13.1 nm 和 13.5 nm 波长处单级次能量为 13.5 nJ 和 11.1 nJ,转换效率为 3.6×10^{-7} 和 3.0×10^{-7} ,光束的空间发散角为 0.32 mrad 和 0.33 mrad。通过实验和模拟研究高能极紫外光束的最佳相位匹配条件,在强场近似框架下,通过考虑传播效应的含时薛定谔方程的数值模型,模拟得到谐波信号随气压和光强的变化趋势(与实验基本相同),结合谐波的空间发散角特性确定了目前激光参数下最优的相位匹配条件。

2 实验装置

实验光路如图 1(a)所示,整个系统被放置在真空中,以避免系统对极紫外脉冲的强烈吸收,真空系统保持 10^{-3} Pa 的背景压力。驱动激光参数为:中心波长 800 nm、重复频率 1 Hz、脉冲宽度 30 fs、能量 35 mJ。使用焦距 $f=5000$ mm 的平凸透镜会聚,焦斑直径约为 $400 \mu\text{m}$,焦点处光强约为 9×10^{14} W/cm²。使用不同孔径的软变光阑来优化光束质量。Ne 注入到长度为 50 mm 的气体盒子中,产生的谐波辐射与基频驱动激光同轴传播。谐波信号经过两个钼(Mo)反射镜和厚度为 350 nm 的锆(Zr)膜,以滤除基频激光场。随后谐波信号通过可移动的镀金球面镜被反射到两个不同的光路中。当球面镜不在光路中时,产生的谐波能量将被极紫外光电二极管探测器测量,该探测器由北京同步辐射装置校准,以得到真实的光谱响应曲线^[27-28]。当球面镜移入光路时,HHG 光谱信息将被平场光栅光谱仪探测。此外,谐波的空间发散角是通过计算信号在极紫外光谱探测器中的纵向分布得到的。

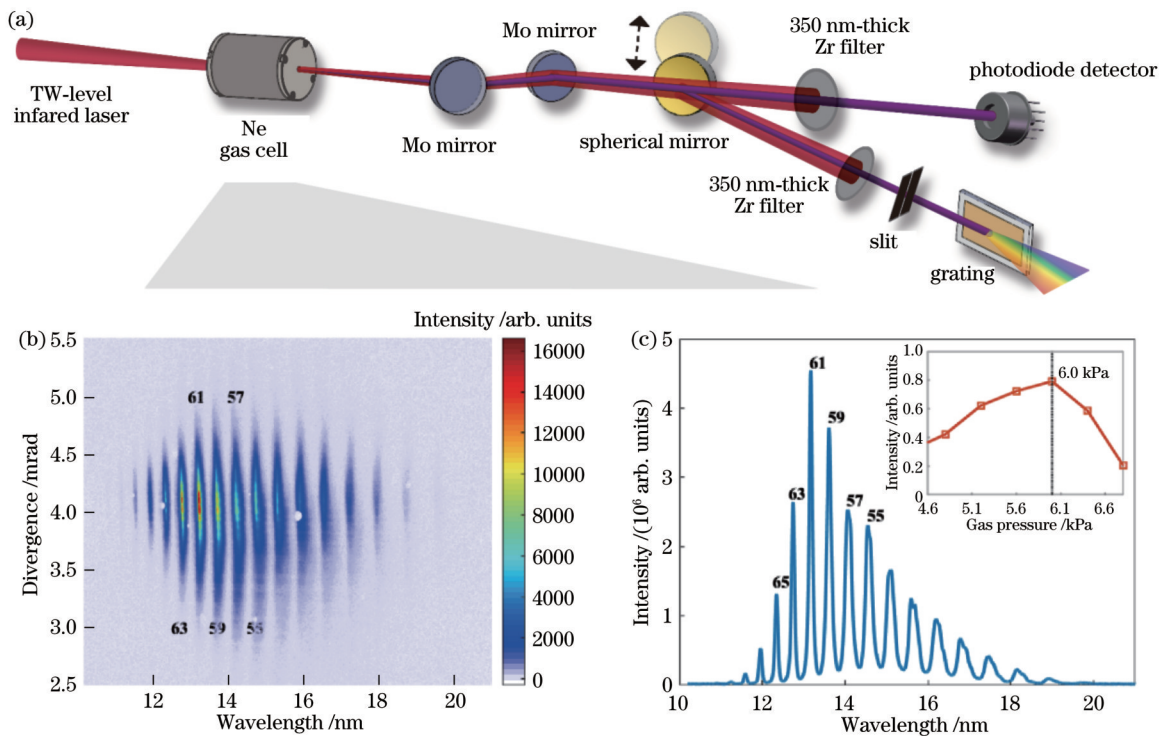


图 1 极紫外脉冲产生。(a)实验光路;(b)高次谐波光谱的空间分布;(c)高次谐波光谱

Fig. 1 Extreme ultraviolet pulse generation. (a) Experimental setup; (b) spatial distribution of high-order harmonic spectrum; (c) high-order harmonic spectrum

3 分析与讨论

图 1(b)、(c)为实验获得的高次谐波光谱,其中,黑色文本表示相应的谐波级次,插图为优化的相位匹配气压。优化的 Ne 气压为 6.0 kPa。为了获得谐波的绝对能量,对极紫外脉冲的透射率和反射率进行了校

准^[29],两块 Mo 镜的反射率约为 42%,Zr 膜的透射率约为 20%。最终获得第 41 级次到第 69 级次(19.5 nm 到 11.6 nm 波长)的 HHG 光谱,其总能量为 78.7 nJ。针对 13 nm 波段的两个级次进行谐波特性分析,根据采集的 HHG 光谱分布得到每个级次所占能量的比值,因此第 61 级次(13.1 nm 波长)和第 59 级次(13.5 nm

波长)的单级次谐波能量分别为 13.5 nJ 和 11.1 nJ, 经过计算得到相应谐波的转换效率为 3.6×10^{-7} 和 3.0×10^{-7} 。谐波的发散角半高全宽 (FWHM) 为 0.32 mrad 和 0.33 mrad, 这也表明所提方案实现了优化的相位匹配条件。为了进一步使用这种高能量的 HHG 源, 例如作为全相干自由电子激光种子源和其他极紫外实验光源, 可以使用极紫外多层膜反射镜^[30] [如 Mo/铍 (Be)^[31]、Mo/硅 (Si)^[32] 和 铷 (Ru)/Si^[33] 等] 来选择特定波长区域的单级次谐波, 得到单色性好的极紫外光源。

产生的高次谐波光子数 N_q 可以通过一维模型简单地描述^[34-35], 表示为

$$N_q \propto S_w (PL_{\text{med}})^2, \quad (1)$$

式中: S_w 为束腰光斑面积, 与透镜焦距成正比; P 为气压; L_{med} 为介质长度。由式 (1) 可知, 对于高能量的 HHG 光源, 利用松聚焦几何结构来增加激光焦斑的面积可以提高谐波光子的产率。要使式 (1) 成立也必须满足两个条件, 即

$$L_{\text{med}} > 3L_{\text{abs}}, L_{\text{coh}} > L_{\text{abs}}, \quad (2)$$

式中: L_{abs} 为吸收长度; L_{coh} 为相干长度。因此, 在当前实验条件下, 第 61 级次和第 59 级次谐波的吸收长度 L_{abs} ^[36] 分别约为 1.53 mm 和 1.47 mm, 介质长度 $L_{\text{med}} = 50$ mm。相干长度 $L_{\text{coh}} = \pi/\Delta k$, 其中, Δk 是总相位失配, 它与中性原子的相位失配 Δk_a 、自由电子的相位失配 Δk_f 、激光场的相位失配 Δk_g 和原子相位失配 Δk_i 的总和有关, 即:

$$\Delta k = \Delta k_a + \Delta k_f + \Delta k_g + \Delta k_i. \quad (3)$$

对于第 61 级次谐波, L_{coh} 大约为 9.4 mm, 满足式 (2) 中的关系。上述用于计算相干长度的参数为: 气压 6.0 kPa、电离率 1%、激光聚焦束腰半径 200 μm 。相干长度 L_{coh} 在 HHG 转换效率中起着重要作用, 这意味着应该针对不同的实验参数对相位匹配条件进行优化调整。相位匹配条件同时包含轴向和径向相位匹配^[34], 轴向相位匹配主要与谐波的时间相干性有关, 气体盒子中沿激光光轴上的每个点都会产生谐波, 考虑到极紫外辐射被气体吸收的影响, 谐波信号主要产生在气体盒子的后部。径向相位匹配主要与空间相干性有关, 谐波产生时若满足相位匹配条件, 产生的光束质量最好, 即空间相干性最高, 此时谐波最接近入射基频激光的空间模式分布, 同时谐波的发散角也最小^[22, 37-40]。实现优化的轴向和径向相位匹配条件既能保证高的谐波产量输出, 又能得到好的光束质量。

为了获得 13 nm 波段优化的 HHG 极紫外光源, 从实验和理论两个方面研究了 Ne 中产生的第 61 级次和第 59 级次谐波强度与气压和驱动激光能量的变化关系, 如图 2(a)~(h) 所示。图 2(a)(e) 显示了实验中谐波强度随激光强度和焦点位置的变化情况, 其中, 负位置表示焦点在气体盒子前, 此时气压固定在 3.3 kPa。

随着激光强度的增加, 第 61 级次和第 59 级次最佳相位匹配位置均向负方向移动, 当入射激光强度在 9×10^{14} W/cm² 左右时, 谐波信号最强。随后研究了在该强度下气压的变化, 如图 2(c)(g) 所示, 可以看出: 存在两个最佳相位匹配气压, 对于第 61 级次, 为 -100 mm 位置处的 6.0 kPa 和 -160 mm 位置处的 7.6 kPa; 第 59 级次最佳气压范围与第 61 级次相似, 但相位匹配允许的气压较第 61 级次更大。理论分析基于强场近似框架下含时薛定谔方程的数值解, 对微观原子偶极响应进行数值模拟, 通过三维麦克斯韦方程组处理谐波产生后涉及的传播效应, 同时考虑气体自身吸收效应的影响。模拟中激光参数和气体介质长度根据实验参数进行设置, 极紫外波段的吸收系数选取参考文献^[41] 中的值。激光场的参数如下: 波长、束腰和脉冲宽度分别设定为 800 nm、180 μm 和 30 fs。图 2(b)、(f) 模拟了谐波强度随驱动激光强度和焦点位置的变化情况, 此时气压为 3.3 kPa。随着激光强度的增加, 气体的电离率会随之增加, 当气体的电离率超过最佳电离率时会导致更大的相位失配, 最终导致 HHG 的退化, 因此, 最佳相位匹配光强的位置向负方向发生移动。根据这一趋势, 在实验条件允许的情况下, 离焦位置能够产生高能极紫外脉冲^[22-23]。但是从实验的角度出发, 在百太瓦激光系统中, 离开束腰位置后, 激光束的空间质量也会迅速退化, 这是一个非常重要的问题。尤其当透镜的焦距为几十米时, 为了在离焦位置获得更高的极紫外脉冲能量, 必须进行光束质量的优化^[25]。图 2(d)、(h) 模拟了谐波强度随气压和焦点位置的变化情况。模拟中激光强度为 5×10^{14} W/cm²。可以看出: 存在三个最佳相位匹配条件的范围, 并且随着气压的增加, 相位匹配位置也向负方向移动。第 61 级次在 0 焦点位置最佳气压为 3.3 kPa, 在 -60 mm 焦点位置最佳气压为 4.7 kPa, 在 -100 mm 焦点位置最佳气压约为 7.3 kPa。第 59 级次与第 61 级次相位匹配气压基本相同, 但其气压的匹配范围更广。

13 nm 波段的谐波强度随气压和光强的变化趋势与实验结果基本符合。当气压不变时, 谐波强度随着激光光强的增加向远离焦点位置的区域变化; 当光强不变时, 距离焦点越远的位置所需要的相位匹配气压越高, 并且在远离焦点位置均出现两个谐波较强的区域。但是实验和理论结果还是存在一些差异, 如: 1) 实现最佳相位匹配条件时的焦点位置不同; 2) 模拟中存在激光强度差异; 3) 模拟结果在焦点位置 0 处出现谐波强度极大值 [图 2(h)]。分析原因如下: 1) 实验中气体盒子的定位误差导致实验和理论得到的焦点位置存在差异; 2) 模拟中的气体分布与实际情况并不完全相同, 实验中谐波产生位置的气压低于测量的值; 3) 数据采集过程中激光参数 (脉宽、能量和光束质量等) 变化会引起误差。综上所述, 忽略这些差异后, 对于上述信号强度随气压和光强的变化趋势以及最佳的相位匹配

条件的取值范围,理论模拟与实验结果基本符合。

根据经典理论^[42]和量子理论^[15],HHG 光谱的物理特性可以用电子的长、短轨道来解释。当电子沿着不同的轨道返回母核粒子,并以不同的能量和相位与之

重新结合时,对应辐射出的光子具有不同的发散角。这意味着 HHG 发散角中包含关于电子轨道贡献的信息,并且短轨道通常比长轨道具有小得多的发散角^[18]。为了获得低发散角的谐波光束,有必要增强短轨道并

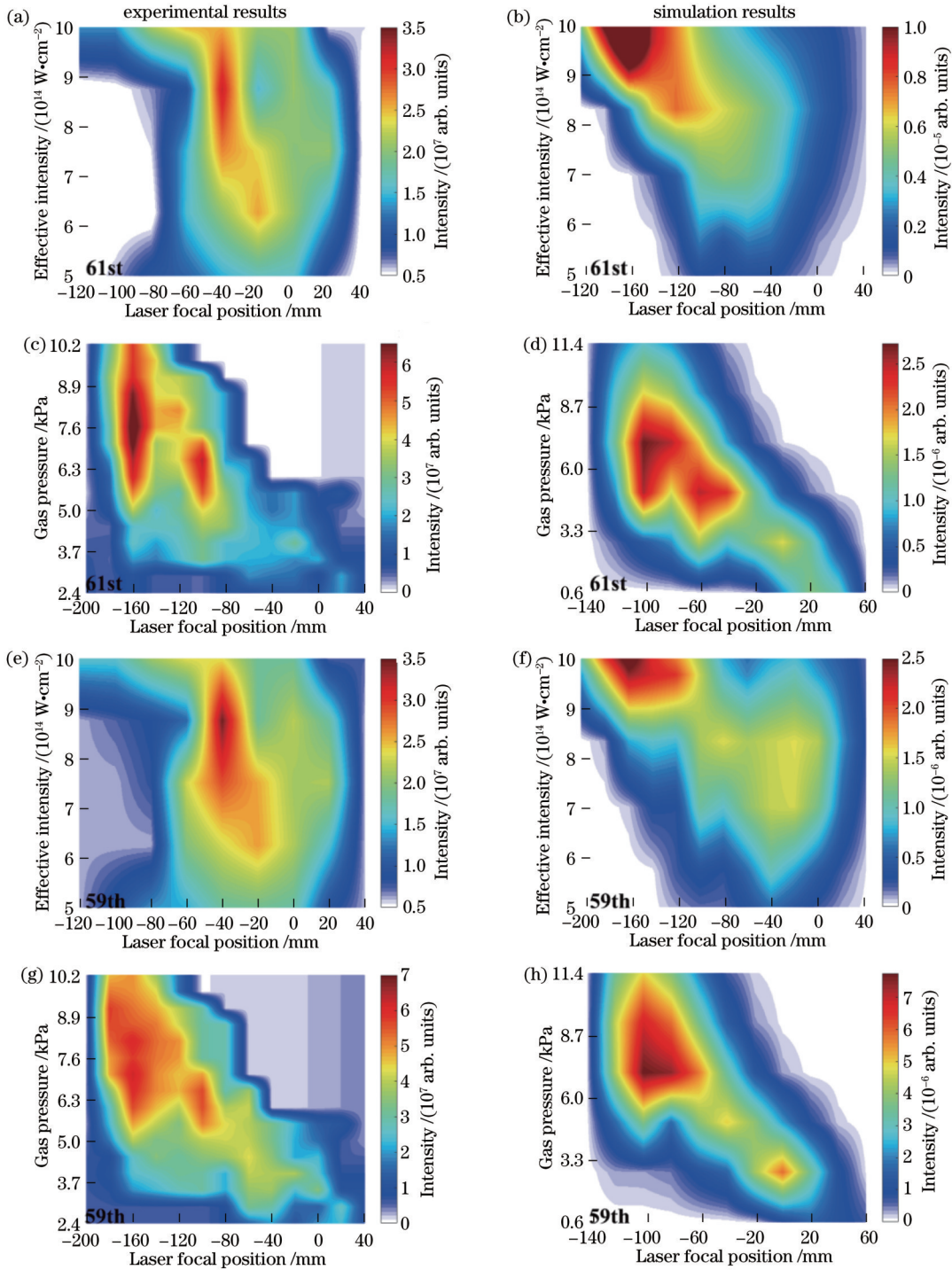


图 2 Ne 中产生第 61 级次和第 59 级次谐波强度随驱动激光强度和气压的变化情况(负位置表示气体盒子位于焦点之后,数据均经插值处理)。(a)(b)谐波强度与驱动激光强度的关系(第 61 级次);(c)(d)谐波强度与气压的关系(第 61 级次);(e)(f)谐波强度与驱动激光强度的关系(第 59 级次);(g)(h)谐波强度与气压的关系(第 59 级次)

Fig. 2 Generation of the 61st and 59th order harmonics in Ne varies with the driving laser energy and gas pressure (negative position indicates that the gas box is located behind the focal point, and the data has been interpolated). (a)(b) Harmonic generated as a function of driving laser energy (61st); (c)(d) harmonic generated as a function of gas pressure (61st); (e)(f) harmonic generated as a function of driving laser energy (59th); (g)(h) harmonic generated as a function of gas pressure (59th)

抑制长轨道。在实验中,通过调整激光焦点相对于气体盒子的位置,可以容易地控制来自不同轨道的贡献比例。当气体盒子放置在激光焦点后的位置时,与长轨道相比,短轨道得到了增强^[43-44]。结合图2的实验结果和理论模拟结果,选取谐波信号出现极大值的三个不同焦点位置的光谱进行分析,图3为不同焦点位置 HHG 的空间分布,其中:灰色阴影区域和橙色虚线分别表示实验数据和 Gaussian 拟合结果;第一行到第三行的焦点位置、气压和激光入射能量的实验参数分别为 0/3.3 kPa/35 mJ、-100 mm/6.0 kPa/35 mJ 和 -160 mm/8.7 kPa/35 mJ。图3(a)~(c)是在焦点位置 0 处的结果,第 61 级次和第 59 级次的谐波发散角分别约为 0.30 mrad 和 0.31 mrad。图3(d)~(f)是在焦点位置 -100 mm 处的结果,第 61 级次和第 59 级次的

谐波发散角分别约为 0.32 mrad 和 0.33 mrad。图3(g)~(i)是在焦点位置 -160 mm 处的结果,第 61 级次和第 59 级次的谐波发散角分别约为 0.57 mrad 和 0.65 mrad。分别对光谱纵向空间分布进行高斯曲线拟合,拟合结果与实际分布较为一致,这也表明了激光沿径向方向实现了相位匹配条件,得到了高光束质量、低发散角的高次谐波辐射。此外,对于焦点位置 0 和 -100 mm 处的谐波分布,曲线的拟合结果优于焦点位置 -160 mm 处。同时需要说明的是,空间分布的拟合结果中,焦点位置 0 和 -100 mm 处拟合的偏差主要出现在两边的旁瓣处,这主要来自“长轨道”的贡献,导致信号的发散角变大,从而使谐波的纵向分布出现略长的“拖尾”,该特征在 HHG 光谱中是较为常见的^[20,44]。因此,实验中并未得到完美的高斯形状分布。

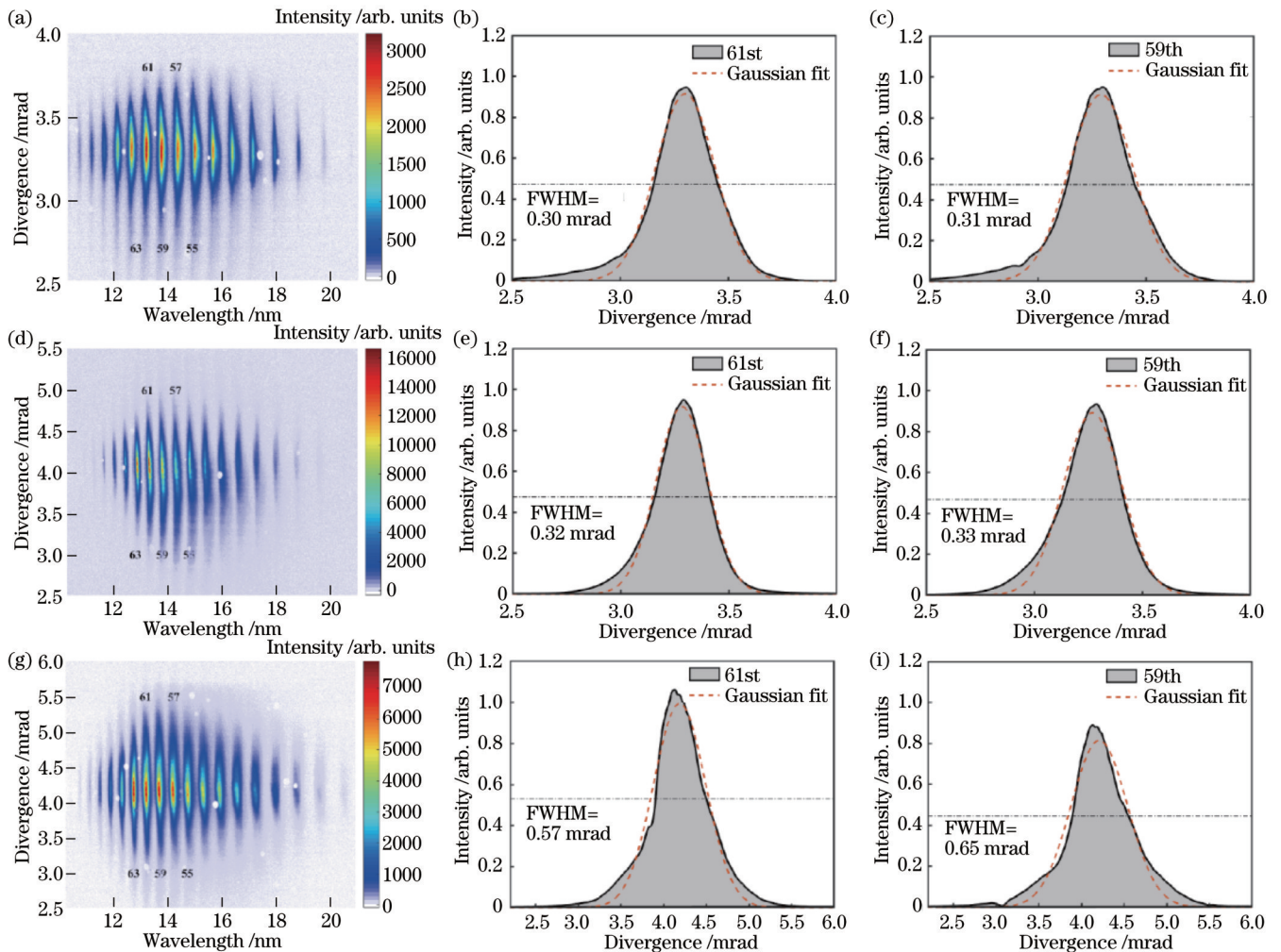


图3 高次谐波的空间分布。(a) 高次谐波光谱(焦点位置为0);(b)(c) 图3(a)对应的第61级次和第59级次谐波的纵向空间轮廓;(d) 高次谐波光谱(焦点位置为-100 mm);(e)(f) 图3(d)对应的第61级次和第59级次谐波的纵向空间轮廓;(g) 高次谐波光谱(焦点位置为-160 mm);(h)(i) 图3(g)对应的第61级次和第59级次谐波的纵向空间轮廓

Fig. 3 Spatial distributions of high-order harmonics. (a) High-order harmonic spectrum (focal position is 0); (b)(c) spatial profiles of 61st and 59th order harmonics corresponding to Fig. 3(a); (d) high-order harmonic spectrum (focal position is -100 mm); (e)(f) spatial profiles of 61st and 59th order harmonics corresponding to Fig. 3(d); (g) high-order harmonic spectrum (focal position is -160 mm); (g)(i) spatial profiles of 61st and 59th order harmonics corresponding to Fig. 3(g)

综上所述,结合图 2 和图 3 的结果,对于 13 nm 波段谐波产生,存在两个信号强度极大值,即 -100 mm 和 -160 mm 焦点位置处。通过调节气压和入射光强可得到优化的相位匹配条件。对于谐波的空间分布来说,-100 mm 焦点位置处谐波的空间分布更接近高斯形状分布。这是因为在 -160 mm 焦点位置,入射激光的空间质量发生退化,导致产生的谐波空间质量也发生退化,进而使谐波的发散角变大。虽然在该位置处也能保证高能量的 13 nm 波段辐射输出,但光束质量略低。因此,选择 -100 mm 焦点位置作为最优相位匹配的结果,相应的参数为最优相位匹配参数。

4 结 论

在与自由电子激光同源的 200 TW 激光系统平台下进行了 HHG 极紫外光源优化工作,以便于其将来作为自由电子激光的种子光源同步注入。总的来说,通过松聚焦的结构获得了低发散角、高转换效率的极紫外脉冲,11.6~19.5 nm 波长光谱范围的总能量为 78.7 nJ。结合实验和模拟结果,通过优化激光能量和气压等参数获得了相位匹配条件随焦点位置的变化情况,同时测量了在不同焦点位置处谐波信号的纵向空间分布。通过数值拟合证明了光谱是较好的高斯分布,且发散角最小约为 0.30 mrad。这两方面的结果证明,实现了在目前激光参数下的最优相位匹配条件。

未来,将使用可变形镜、波前传感器等波前校正技术^[25,45]来进一步优化光束质量,同时可使用更高重复频率的驱动激光来提高谐波的平均功率。这在强阿秒脉冲产生、极紫外泵浦探测和自由电子激光种子源注入等方面将有重要的应用前景。

参 考 文 献

- [1] Mairesse Y, Bohan A D, Frasinski L J, et al. Attosecond synchronization of high-harmonic soft X-rays[J]. *Science*, 2003, 302(5650): 1540-1543.
- [2] 戴晨, 汪洋, 缪志明, 等. 基于飞秒激光与物质相互作用的高次谐波产生及应用[J]. *激光与光电子学进展*, 2021, 58(3): 0300001.
Dai C, Wang Y, Miao Z M, et al. Generation and application of high-order harmonics based on interaction between femtosecond laser and matter[J]. *Laser & Optoelectronics Progress*, 2021, 58(3): 0300001.
- [3] Labat M, Bellaveglia M, Bougeard M, et al. High-gain harmonic-generation free-electron laser seeded by harmonics generated in gas[J]. *Physical Review Letters*, 2011, 107(22): 224801.
- [4] Zeitoun P, Faivre G, Sebban S, et al. A high-intensity highly coherent soft X-ray femtosecond laser seeded by a high harmonic beam[J]. *Nature*, 2004, 431(7007): 426-429.
- [5] Sie E J, Rohwer T, Lee C M, et al. Time-resolved XUV ARPES with tunable 24–33 eV laser pulses at 30 meV resolution[J]. *Nature Communications*, 2019, 10: 3535.
- [6] Tanksalvala M, Porter C L, Esashi Y, et al. Nondestructive, high-resolution, chemically specific 3D nanostructure characterization using phase-sensitive EUV imaging reflectometry[J]. *Science Advances*, 2021, 7(5): eabd9667.

- [7] Hettel R. DLSR design and plans: an international overview[J]. *Journal of Synchrotron Radiation*, 2014, 21(5): 843-855.
- [8] Elias L R, Fairbank W M, Madey J M J, et al. Observation of stimulated emission of radiation by relativistic electrons in a spatially periodic transverse magnetic field[J]. *Physical Review Letters*, 1976, 36(13): 717-720.
- [9] Wang W T, Feng K, Ke L T, et al. Free-electron lasing at 27 nanometres based on a laser Wakefield accelerator[J]. *Nature*, 2021, 595(7868): 516-520.
- [10] 齐争, 黄楠顺, 邓海啸, 等. 上海硬 X 射线自由电子激光装置光源性能参数与稳定性研究[J]. *光学学报*, 2022, 42(11): 1134016.
Qi Z, Huang N S, Deng H X, et al. Performance parameters and stability studies on FEL-III beamline of Shanghai high repetition rate XFEL and extreme light facility[J]. *Acta Optica Sinica*, 2022, 42(11): 1134016.
- [11] Matthews D L, Hagelstein P L, Rosen M D, et al. Demonstration of a soft X-ray amplifier[J]. *Physical Review Letters*, 1985, 54(2): 110-113.
- [12] Key M H. Laboratory production of X-ray lasers[J]. *Nature*, 1985, 316(6026): 314-319.
- [13] Cerjan C. Spectral characterization of a Sn soft X-ray plasma source[J]. *Journal of Applied Physics*, 1994, 76(6): 3332-3336.
- [14] Ditmire T, Gumbrell E T, Smith R A, et al. Spatial coherence measurement of soft X-ray radiation produced by high order harmonic generation[J]. *Physical Review Letters*, 1996, 77(23): 4756-4759.
- [15] Popmintchev T, Chen M C, Arpin P, et al. The attosecond nonlinear optics of bright coherent X-ray generation[J]. *Nature Photonics*, 2010, 4(12): 822-832.
- [16] Popmintchev D, Hernández-García C, Dollar F, et al. Ultraviolet surprise: efficient soft X-ray high-harmonic generation in multiply ionized plasmas[J]. *Science*, 2015, 350(6265): 1225-1231.
- [17] Bartels R A, Paul A, Green H, et al. Generation of spatially coherent light at extreme ultraviolet wavelengths[J]. *Science*, 2002, 297(5580): 376-378.
- [18] Popmintchev T, Chen M C, Popmintchev D, et al. Bright coherent ultrahigh harmonics in the keV X-ray regime from mid-infrared femtosecond lasers[J]. *Science*, 2012, 336(6086): 1287-1291.
- [19] Zhang X, Libertun A R, Paul A, et al. Highly coherent light at 13 nm generated by use of quasi-phase-matched high-harmonic generation[J]. *Optics Letters*, 2004, 29(12): 1357-1359.
- [20] Lewenstein M, Balcou P, Ivanov M Y, et al. Theory of high-harmonic generation by low-frequency laser fields[J]. *Physical Review A*, 1994, 49(3): 2117-2132.
- [21] Milosevic N, Scrinzi A, Brabec T. Numerical characterization of high harmonic attosecond pulses[J]. *Physical Review Letters*, 2002, 88(9): 093905.
- [22] Takahashi E J, Nabekawa Y, Midorikawa K. Low-divergence coherent soft X-ray source at 13 nm by high-order harmonics[J]. *Applied Physics Letters*, 2004, 84(1): 4-6.
- [23] Rudawski P, Heyl C M, Brizuela F, et al. A high-flux high-order harmonic source[J]. *Review of Scientific Instruments*, 2013, 84(7): 073103.
- [24] Wang Y, Guo T Y, Li J L, et al. Enhanced high-order harmonic generation driven by a wavefront corrected high-energy laser[J]. *Journal of Physics B: Atomic, Molecular and Optical Physics*, 2018, 51(13): 134005.
- [25] Li J L, Wang Y, Guo T Y, et al. Beam optimization in a 25 TW femtosecond laser system for high harmonic generation[J]. *Journal of Physics B: Atomic, Molecular and Optical Physics*, 2020, 53(14): 145602.
- [26] Xu Y, Lu J, Li W K, et al. A Stable 200 TW/1 Hz Ti:sapphire laser for driving full coherent XFEL[J]. *Optics & Laser Technology*, 2016, 79: 141-145.

- [27] Ranc S, Chériaux G, Ferré S, et al. Importance of spatial quality of intense femtosecond pulses[J]. Applied Physics B, 2000, 70(1): S181-S187.
- [28] Zhang L Y, Zheng Y H, Li G C, et al. Bright high-order harmonic generation around 30 nm using hundred-terawatt-level laser system for seeding full coherent XFEL[J]. Applied Sciences, 2018, 8(9): 1446.
- [29] Lou Z Y, Zheng Y H, Zhang L Y, et al. Bright high harmonic generation around 30 nm and 10 nm for seeding full coherent XFEL[J]. Proceedings of SPIE, 2019, 11056: 110562M.
- [30] 王占山, 黄秋实, 张众, 等. 极紫外、X射线和中子薄膜光学元件与系统[J]. 光学学报, 2021, 41(1): 0131001.
Wang Z S, Huang Q S, Zhang Z, et al. Extreme ultraviolet, X-ray and neutron thin film optical components and systems[J]. Acta Optica Sinica, 2021, 41(1): 0131001.
- [31] Bogachev S A, Chkhalo N I, Kuzin S V, et al. Advanced materials for multilayer mirrors for extreme ultraviolet solar astronomy[J]. Applied Optics, 2016, 55(9): 2126-2135.
- [32] Ichimaru S, Hatayama M, Ohchi T, et al. Mo/Si multilayer mirrors with 300-bilayers for EUV lithography[J]. Proceedings of SPIE, 2015, 9658: 965814.
- [33] Li O W, Wong K, Parks V, et al. Improved Ru/Si multilayer reflective coatings for advanced extreme-ultraviolet lithography photomasks[J]. Proceedings of SPIE, 2016, 9776: 977619.
- [34] Constant E, Garzella D, Breger P, et al. Optimizing high harmonic generation in absorbing gases: model and experiment [J]. Physical Review Letters, 1999, 82(8): 1668-1671.
- [35] Takahashi E J, Nabekawa Y, Mashiko H, et al. Generation of strong optical field in soft X-ray region by using high-order harmonics[J]. IEEE Journal of Selected Topics in Quantum Electronics, 2004, 10(6): 1315-1328.
- [36] Henke B L, Gullikson E M, Davis J C. X-ray interactions: photoabsorption, scattering, transmission, and reflection at $E=$ 50–30, 000 eV, $Z=1-92$ [J]. Atomic Data and Nuclear Data Tables, 1993, 54(2): 181-342.
- [37] Hernández-García C, Sola I J, Plaja L. Signature of the transversal coherence length in high-order harmonic generation [J]. Physical Review A, 2013, 88(4): 043848.
- [38] Durfee C G, Rundquist A R, Backus S, et al. Phase matching of high-order harmonics in hollow waveguides[J]. Physical Review Letters, 1999, 83(11): 2187-2190.
- [39] Takahashi E, Nabekawa Y, Midorikawa K. Generation of 10- μ J coherent extreme-ultraviolet light by use of high-order harmonics [J]. Optics Letters, 2002, 27(21): 1920-1922.
- [40] Takahashi E, Tosa V, Nabekawa Y, et al. Experimental and theoretical analyses of a correlation between pump-pulse propagation and harmonic yield in a long-interaction medium[J]. Physical Review A, 2003, 68(2): 023808.
- [41] Physical Measurement Laboratory, National Institute of Standards and Technology, U. S. Department of Commerce. Elemental data index[EB/OL]. [2004-07]. <https://physics.nist.gov/cgi-bin/Elements/elInfo.pl?element=10&context=frames>.
- [42] Corkum P B. Plasma perspective on strong field multiphoton ionization[J]. Physical Review Letters, 1993, 71(13): 1994-1997.
- [43] Salières P, L'Huillier A, Lewenstein M. Coherence control of high-order harmonics[J]. Physical Review Letters, 1995, 74(19): 3776-3779.
- [44] He X K, Miranda M, Schwenke J, et al. Spatial and spectral properties of the high-order harmonic emission in argon for seeding applications[J]. Physical Review A, 2009, 79(6): 063829.
- [45] 胡逸雯, 刘鑫, 匡翠方, 等. 基于深度学习的自适应光学技术研究进展及展望[J]. 中国激光, 2023, 50(11): 1101009.
Hu Y W, Liu X, Kuang C F, et al. Research progress and prospect of adaptive optics based on deep learning[J]. Chinese Journal of Lasers, 2023, 50(11): 1101009.

High-Energy High-Order Harmonic Generation Around 13 nm Wavelength Based on Hundred-Terawatt-Level Laser System

Gao Jixing^{1,2}, Lou Zhiyuan^{1,2}, Yang Fan^{1,2}, Yang Xiaojun¹, Xu Yi^{1,2}, Leng Yuxin^{1,2},
Zheng Yinghui^{3*}, Zeng Zhinan³, Li Ruxin^{1,2,3}

¹State Key Laboratory of High Field Laser Physics, Shanghai Institute of Optics and Fine Mechanics, Chinese Academy of Sciences, Shanghai 201800, China;

²Center of Materials Science and Optoelectronics Engineering, University of Chinese Academy of Sciences, Beijing 100049, China;

³Zhangjiang Laboratory, Shanghai 201210, China

Abstract

Objective With the rapid development of high-order harmonic extreme ultraviolet coherent light sources and attosecond pulses, they have caught widespread attention in free electron laser seed injection, time-resolved angular resolved photoelectron spectroscopy measurement, and nondestructive nanostructure detection. There are many ways to generate extreme ultraviolet light sources, including synchrotron radiation, laser produced plasma, and free electron lasers, which can also be employed to generate high-energy extreme ultraviolet light sources. Compared to other light sources, high-order harmonics feature good coherence, short pulse duration, and device miniaturization. Currently, the high-order harmonic mechanism has been widely adopted to generate coherent light sources in the extreme ultraviolet region. We utilize a self-developed 200 TW titanium sapphire laser system with a maximum single pulse energy that can reach 8 J, and a main pulse energy of 7.9 J after beam splitting is transported to the free electron laser experiment for generating an

electron beam source based on the acceleration mechanism of laser wakefield. The second laser beam is leveraged for high-order harmonic generation experiments. Both experiments are conducted synchronously to facilitate the simultaneous injection of electron beams and extreme ultraviolet seed beams into the oscillators in the future.

Methods As shown in Fig. 1(a), the whole system is placed in a vacuum chamber to avoid strong absorption of extreme ultraviolet pulse, and the vacuum system maintains the background pressure of 10^{-3} Pa. The driving laser parameters include a center wavelength of 800 nm, repetition rate of 1 Hz, pulse width of 30 fs, and energy of 35 mJ. A plano-convex mirror with a focal length of 5000 mm and a focal spot diameter of about 400 μm is adopted. The length of the Ne-filled gas cell is 50 mm. The harmonic radiation propagates with the residual driving laser and then transmits through the iris to the measurement section. Two Mo mirrors and a 350 nm-thick Zr filter are placed behind the iris to attenuate the fundamental laser field. Then, the harmonic signals can be divided into two different paths via the moveable gold-coated spherical mirror. Absolute harmonic energy is measured with an XUV (extreme ultra violet) photodiode detector which is calibrated by the Beijing Synchrotron Radiation Facility to get the real spectrum response curve. When the spherical mirror moves into the beam path, the HHG (high-order harmonic generation) spectrum is detected by a home-built flat-filied grating spectrometer. The spatial harmonic distribution is obtained by calculating the longitudinal spectrum of the XUV charge-coupled device.

Results and Discussions Figures 1(b) and 1(c) show the generated harmonic spectra. From the 41st to the 69th harmonics (19.5 nm to 11.6 nm wavelength), the total energy of HHG is about 78.7 nJ. According to the HHG spectral distribution, the single harmonic energy of the 61st harmonic (13.1 nm) and 59th harmonic (13.5 nm) is 13.5 nJ and 11.1 nJ, respectively. The conversion efficiency is 3.6×10^{-7} for 61st harmonic and 3×10^{-7} for 59th harmonic. The divergence of the output beam measured at 61st and 59th harmonics is about 0.32 mrad and 0.33 mrad (full width at half maxima, FWHM). To obtain the optimal HHG extreme ultraviolet source at the wavelength of 13 nm, we investigate the 61st and the 59th harmonic intensity generated in Ne as a function of the gas pressure and driving laser energy. Figures 2(a) and 2(e) present the optimal phase-matching conditions for driving laser energy with the position of gas cell. With the increasing laser energy, the optimal phase-matching position moves to the negative position. Then the optimal phase-matching conditions for the gas pressure at 9×10^{14} W/cm² are studied. As shown in Figs. 2(c) and 2(g), two optimal phase-matching conditions for 61st harmonic are 6.0 kPa at -100 mm position and 7.6 kPa at -160 mm position, respectively. The optimal gas pressure for the 59th and 61st harmonics is basically the same, but 59th harmonic matching range of gas pressure is wider, with the matching gas pressure slightly higher than that for the 61st harmonic. Figures 2(b), 2(d), 2(f), and 2(h) demonstrate the theoretical results in Ne that generates harmonics as a function of driving laser energy and gas pressure respectively. Based on the experimental and theoretical simulation results in Fig. 2, the spectra of three different focal positions with maximum harmonic signals are selected for analysis in Fig. 3, which shows the harmonic spectra at different focal positions. The beam divergence of the 61st and the 59th harmonics is about 0.30 mrad and 0.31 mrad at position of 0, 0.32 mrad and 0.33 mrad at position of -100 mm, and 0.57 mrad and 0.65 mrad at position of -160 mm. The fitting results of harmonic distribution and curve at positions 0 and -100 mm are better than those at -160 mm. Additionally, the Gaussian-like distribution shows that the phase-matching conditions are well achieved. The simulated changes in gas pressure and driving laser energy in phase-matching conditions are basically the same as the experimental results. Finally, the optimal phase-matching conditions for the current laser parameters are obtained by combining the longitudinal distribution of the 13 nm spectra obtained at different focal positions. Combined with the experimental and simulation results, the relationship between phase-matching conditions and focal positions is realized by optimizing parameters such as driving laser energy and gas pressure. Meanwhile, the longitudinal spatial distribution of harmonic signals at different focal positions is measured, and numerical fitting proves that the spectrum has a good Gaussian distribution with a minimum divergence angle of 0.30 mrad. The results combining these two aspects verify that the optimal phase-matching conditions under the current laser parameters are achieved.

Conclusions Extreme ultraviolet pulses with low divergence angle and high conversion efficiency are obtained by loosely focused beams, with a total energy of 78.7 nJ in the spectral wavelength range of 11.6 nm to 19.5 nm. We employ a 200 TW laser system homologous to free-electron lasing (FEL) and optimize the HHG extreme ultraviolet light source under this system platform to facilitate synchronous injection of FEL seed laser. In the future, wavefront correction technologies (such as deformable mirrors and wavefront sensors) will be adopted to further optimize beam quality, and higher repetition frequency lasers can be utilized to increase the average power of harmonics. This will have important application prospects in strong attosecond pulse generation, extreme ultraviolet pump-probe spectroscopy, and FEL seed source injection.

Key words extreme ultraviolet; high-order harmonic; phase matching; spatial distribution